pubs.acs.org/Biomac

Article

Self-Assembly of Unusually Stable Thermotropic Network Phases by Cellobiose-Based Guerbet Glycolipids

Soumi Das, Caini Zheng, Timothy P. Lodge, J. Ilja Siepmann,* Mahesh K. Mahanthappa,* Michelle A. Calabrese,* and Theresa M. Reineke*

Cite This: *Biomacromolecules* 2024, 25, 1291−1302

Read Online

ACCESS | Metrics & More | Article Recommendations | Supporting Information

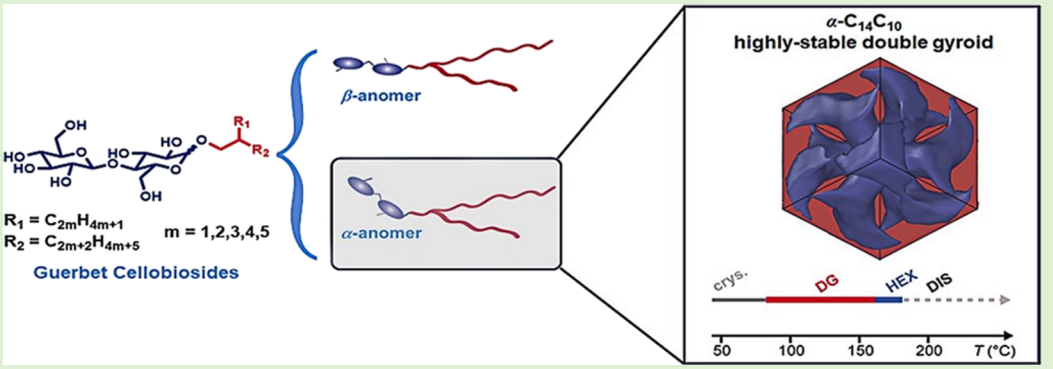

ABSTRACT: Bicontinuous thermotropic liquid crystal (LC) materials, e.g., double gyroid (DG) phases, have garnered significant attention due to the potential utility of their 3D network structures in wide-ranging applications. However, the utility of these materials is significantly constrained by the lack of robust molecular design rules for shape-filling amphiphiles that spontaneously adopt the saddle curvatures required to access these useful supramolecular assemblies. Toward this aim, we synthesized anomerically pure Guerbet-type glycolipids bearing cellobiose head groups and branched alkyl tails and studied their thermotropic LC self-assembly. Using a combination of differential scanning calorimetry, polarized optical microscopy, and small-angle X-ray scattering, our studies demonstrate that Guerbet cellobiosides exhibit a strong propensity to self-assemble into DG morphologies over wide thermotropic phase windows. The stabilities of these assemblies sensitively depend on the branched alkyl tail structure and the anomeric configuration of the glycolipid in a previously unrecognized manner. Complementary molecular simulations furnish detailed insights into the observed self-assembly characteristics, thus unveiling molecular motifs that foster network phase self-assembly that will enable future designs and applications of network LC materials.

INTRODUCTION

Supramolecular network morphologies stemming from the self-assembly of molecular amphiphiles offer opportunities for the bottom-up construction of materials with applications including organic semiconductors and energy storage media,[1] size-selective molecular separations membranes,[2] membrane-bound protein crystallization platforms,[3,4] and internally structured lipid nanoparticles for therapeutic delivery.[5,6] Exemplified by functional bicontinuous double gyroid (DG), double diamond, and other periodic networks, applications of these materials crucially depend on their interpenetrating, labyrinthine nanochannels with tailored chemical constitutions and physical properties. These intricate self-assembled structures are known to arise from thermotropic self-assembly of various liquid crystal (LC) mesogens[7] comprising chemically dissimilar segments of widely varied structures, including polycatenars,[8] rod-like polyphiles,[9,10] wedge-shaped molecules,[11] disk-like molecules,[12] bolamphiphiles,[13,14] and glycolipids.[15−18] However, these thermotropic phases often form only with restricted molecular compositions and in narrow thermal stability windows, since the negative Gaussian ("saddle splay") curvature microdomain interfaces of these assemblies exhibit substantial mean curvature deviations that result in molecular packing frustration.[19−21] The lack of robust molecular designs that drive mesoscale network self-assembly substantially curtails exciting current and future applications of these nanostructures.

Derived from conjugating hydrophilic oligosaccharides to hydrophobic alkyl tails, glycolipids offer a robust platform of

Received: November 17, 2023
Revised: December 1, 2023
Accepted: December 4, 2023
Published: January 3, 2024

https://doi.org/10.1021/acs.biomac.3c01266
Biomacromolecules 2024, 25, 1291−1302

stereochemically well-defined mesogens[15] for exploring how molecular structure directs network phase self-assembly. Broad access to exquisitely tailored LC phases based on sustainable, economical, and biocompatible building blocks furnishes exciting opportunities to develop new materials for commodity applications as well as value-added biological applications.[22] While a few glycolipids are known to form thermotropic mesoscale network LCs,[16,23] insights into how their intricate molecular structures influence their ability to create and stabilize these network phases remain elusive. Although the impact of sugar stereochemistry on glycolipid self-assembly has been examined previously, studies of the influence of glycolipid stereoisomerism on thermotropic phase behavior have primarily focused on monosaccharide-based amphiphiles.[24] Notably, an investigation by Vill et al.[25] explored the stereochemistry-driven thermotropic self-assembly of straight-chain disaccharide-based glycosides. However, phase characterization, especially with respect to identifying cubic network phases, was restricted to imaging via polarized optical microscopy (POM). Accordingly, the specific network phase formed and associated length scales could not be identified. Overall, the limited understanding of how glycolipid stereochemistry affects their ability to form network phases and enhances phase stability across a wide temperature range constrains their full potential for applications. Additionally, glycolipids are extremely hygroscopic, and the presence of water can substantially affect their self-assembled morphologies. These structure and composition variations restrict key insights into the role of molecular shape in governing the supramolecular packings that drive network phase formation.

Herein, we describe the thermotropic LC phase behaviors of a homologous series of diastereomerically pure glycolipids derived from conjugating the disaccharide cellobiose to a branched Guerbet alcohol tail. The specific emphasis on glycolipids of cellobiose, a disaccharide comprising two glucose units linked by a $\beta(1 \rightarrow 4)$ glycosyl bond that is readily obtained from cellulose, is motivated by its known antifungal, antibiotic, and biosurfactant properties.[26] Cellobiose lipids thus hold great potential for applications in the fields of food, medicine, and environmental protection. However, the phase behavior of cellobiose lipids has been minimally explored, with most studies focusing on β-anomers.[25,27] By a judicious choice of synthesis and purification conditions, we isolate anomerically pure α- and β- cellobiosides with varied chain lengths. Using a combination of differential scanning calorimetry (DSC), POM, and high-resolution small-angle X-ray scattering (SAXS), we identify Guerbet cellobiosides that self-assemble into DG phases with exceptionally wide windows of thermal stability. Complementary molecular dynamics (MD) simulations unveil how the anomeric configuration and branched tail structures of these glycolipids lead to their anisotropic conformations that stabilize their saddle curvature packings in thermotropic DG phases.

EXPERIMENTAL SECTION

Materials and Instrumentation. α-D-cellobiose octaacetate (98%), 2-butyl-1-octanol (95%), 2-decyl-1-tetradecanol (97%), $BF_3{\bullet}Et_2O$, $SnCl_4$ (98%), $NaOCH_3$ in CH_3OH, and the ion-exchange resin DOWEX 50WX8-400 were obtained from Millipore-Sigma (Milwaukee, WI). 2-octyl-1-dodecanol and 2-hexyl-1-decanol (>97%) were purchased from TCI Chemicals (Philadelphia, PA), and 2-ethyl-1-hexanol was received from Spectrum Chemical (New Brunswick, NJ). All the received chemicals and reagents were used as received. All the solvents used for this work were of ACS grade. Synthesized compounds were purified via column chromatography using silica gel (60−120 mesh) procured from Millipore-Sigma. The reactions were monitored by thin-layer chromatography (TLC) using plates coated with Silica Gel 60 obtained from Fisher Scientific. NMR solvents were obtained from Millipore-Sigma.

^{1}H NMR and ^{13}C NMR spectra were recorded with Bruker spectrometer at 400 and 150 MHz, respectively, using methanol-d_4 as the solvent. Chemical shifts were referenced to the residual protiated solvent peak, and spectral analyses yielded the reported chemical shifts in δ (ppm) and coupling constants J (Hz). Peak multiplicities are designated as s (singlet), d (doublet), t (triplet), m (multiplet), and br (broadened).

General Glycolipid Synthesis Procedure. Guerbet cellobiosides with varying branched alkyl tail lengths were synthesized in two steps following a well-established procedure, typically starting from alpha-D-cellobiose octaacetate.[25,27,28] We present a representative synthesis of a such compound.

The first step comprised a Lewis acid-mediated direct glycosylation reaction using acetyl-protected cellobiose with a Guerbet alcohol. Reactions using Lewis acid $BF_3{\bullet}Et_2O$ generally yielded 1:2 mixtures of the α- and β-cellobioside peracetates, from which pure β-anomers could be chromatographically isolated. On the other hand, glycosylations mediated by $SnCl_4$ yielded 3:1 mixtures of α- and β-cellobioside peracetates. The latter reaction mixtures were chromatographically separated to yield pure α-anomers.

Briefly, α-D-cellobiose octaacetate (1.5 mmol, 1 equiv) was dissolved with a magnetic stir bar under a nitrogen atmosphere in anhydrous dichloromethane (20 mL). Upon obtaining a homogeneous solution, the selected Lewis acid (7.4 mmol, 5 equiv.) was added. Finally, the desired Guerbet alcohol (2.2 mmol, 1.5 equiv.) was added dropwise to the reaction mixture at 0 °C, and upon completion of alcohol addition, the reaction was brought to ambient temperature gradually and allowed to react for 48 h. The reaction mixture was then diluted with CH_2Cl_2 and quenched with saturated $NaHCO_3$ (aq) followed by extraction with CH_2Cl_2 (3 × 20 mL). The combined organic layers were further washed with saturated NaCl(aq) (15 mL) and dried over anhydrous Na_2SO_4(s). The obtained crude reaction mixture was concentrated by rotary evaporation and purified by column chromatography using an ethyl acetate/hexane solvent system as follows (specific solvent systems are specified with each compound below). The acetyl ester of the respective alkanols, a side product of the reaction, was first eluted with pure hexanes. Subsequently, the desired anomers were collected by using a hexane/ethyl acetate mixture. Depending upon the Guerbet chain length, the ethyl acetate/hexane % v/v also varied from 36% v/v (for − $C_{14}C_{10}$ Guerbet chain) to 42% v/v (for − C_6C_2 Guerbet chain). The first and last few fractions provided pure β- and α-anomers, respectively, whereas the major middle fractions contained a mixture of both anomers. In the case of the $SnCl_4$-mediated reaction, the first few fractions produced the mixture of anomers, and later fractions yielded pure glycolipid anomers. The fractions containing anomerically pure peracetates were isolated, and their purities were confirmed by ^{1}H NMR.

The Guerbet glycolipid peracetates were then deprotected by Zemplén deacetylation as follows.[28] The peracetylated glycolipids were dissolved in MeOH, and the reaction basicity was adjusted to pH 9 with solid NaOMe at 22 °C. Complete deacetylation was indicated by TLC after 16 h. It was followed by ion exchange with Dowex resin (H^+ form). After the removal of the resin by filtration, the desired glycolipids were isolated by concentrating the filtrate. The obtained glycolipids were also characterized by ^{1}H and ^{13}C NMR spectroscopy (Figures S1−S10).

All of the samples were lyophilized for 4 days to exhaustively remove trace water from these hygroscopic compounds.

Elemental Analysis. Lyophilized sample purity was assessed by combustion elemental analyses conducted at Atlantic Microlab (Norcross, GA, USA). The values are provided in the section of characterization data of synthesized compounds in the Supporting Information.

https://doi.org/10.1021/acs.biomac.3c01266
Biomacromolecules 2024, 25, 1291−1302

Differential Scanning Calorimetry. DSC experiments to identify thermotropic transitions employed a Mettler Toledo DSC 1 instrument with cooling accessories operating under N_2(g). DSC samples were prepared by sealing ∼5−8 mg of the lyophilized glycolipids into Tzero aluminum pans (DSC Consumables, Austin, MN). After the samples were equilibrated at 25 °C, DSC data were acquired on heating at 5 °C/min and analyzed using the TA Instruments thermal analysis software. Reported data and thermograms reflect the first sample heating, which clearly exhibited mobility transitions and thermotropic liquid crystalline phase transitions.

Polarized Optical Microscopy. POM studies of LC phase textures employed an Olympus BX53 polarized light microscope, which was equipped with a Linkam LTS420 hot stage and a T95 temperature controller operated by the Linksys 32 software. Digital image capture relied on a QiCam Fast 1394 12-bit camera. Dried glycolipid samples were placed on clean microscope slides. A coverslip with silicone grease applied along the edges was placed on top of the sample to protect it from atmospheric contact to minimize moisture uptake. The samples were heated at a rate of 10 °C/min to a particular temperature and annealed for at least 5 min prior to taking an observation.

Small-Angle X-ray Scattering. *Sample Preparation.* Lyophilized glycolipid samples (30 mg) were hermetically sealed in a TZero aluminum DSC pan (TA Instruments, New Castle, DE, USA) under argon in an inert atmosphere glovebox to prevent unwanted moisture uptake.

Measurement. Variable temperature SAXS analyses were conducted at the 5-ID-D and 12-ID-B beamlines of the Advanced Photon Source (Argonne, IL). Samples were either loaded into a sample array stage available at the beamline that furnished stable temperature control (±3 °C) over the range T = 25−205 °C, or they were thermostated on a Linkam hot stage (±1 °C temperature stability). Samples were heated to a target temperature at a rate of 10 °C/min and thermally equilibrated for at least 10 min prior to X-ray exposure.

Analyses conducted at the 5-ID-D beamline employed an 8.5 sample-to-detector distance (SDD) with a beam energy of 17 keV, while experiments at the 12-ID-B beamline used a 3.6 m SDD with 12 keV beam energy. In both cases, flight tubes for the incident and scattered beams were under vacuum to minimize air scattering. At the 5-ID-D beamline, 2D-SAXS patterns were obtained using a series of three annular Rayonix MX170-HS detectors with 3840 × 3840 resolution (86.6 × 86.6 μm pixels) with a 170 × 170 mm^2 active area. At the 12-ID-B beamline, 2D-SAXS patterns were collected on a Pilatus 2M detector with 1475 × 1679 resolution (172 × 172 μm^2 pixels) with 253.7 × 288.8 mm^2 active area and 2D-WAXS patterns were obtained using a Pilatus 300K detector 487 × 619 resolution (172 × 172 μm^2 pixels) with 33.5 × 83.8 mm^2 active area. These conditions enabled the acquisition of scattering patterns over a range of scattering wavevector values of $0.003 \leq |\boldsymbol{q}| \leq 0.5$ Å^{-1}. To ensure sample homogeneity at each temperature, five 2D-SAXS patterns were recorded at different locations in each sample pan.

The 2D scattering data were azimuthally integrated to obtain the scattered intensity $I(q)$ as a function of $|\boldsymbol{q}| = 4\pi\sin(\theta/2)/\lambda$, where θ is the scattering angle and λ is the incident beam wavelength. The presented SAXS data (Figure S12−S17) is in its original form without any background subtraction and the Bragg peaks for ordered morphologies were indexed with a freely available 1D-SAXS indexing macro for Igor Pro.[29]

Calculation of Volume Fractions. The volume fraction of the lipid tail (ϕ_l) can be determined using the equation $\phi_l = V_{tail}/(V_{tail} + V_{head})$, where V_{tail} and V_{head} refer to the molar volume of the lipid tail and headgroup, respectively. However, to the best of our knowledge, temperature-dependent data for the molar volume or the specific density of glycolipids are lacking, nor have the volume contributions from the lipid tail and sugar head groups been determined. In pioneering work on the packing of glycolipids, Nguan et al.[30] suggested specific densities of 1.5 g/cm^3 and 0.8 g/cm^3 for the sugar head and lipid tail, respectively, at room temperature based on experimental data for crystalline or amorphous sugars and paraffins. Nguan et al. also suggested density−temperature coefficients with values of "$\Delta\rho(T) = -0.06$ g m^{-1} K^{-1} for the sugar and −0.1 g m^{-1} K^{-1} for the paraffin"[30] but these latter values appear problematic with regard to units and magnitude. Here, we present density calculations based on data from our MD simulations in the isobaric−isothermal ensemble. The MD simulations were conducted for α- and β-anomers with four different tail lengths at three temperatures (390, 420, and 450 K) at 1 bar. The simulations were equilibrated for 500 ns, and ensemble averages were obtained over an additional period of 100 ns. The values for the specific density are reported in Table S4. Assuming no volume change upon mixing, the total volume of a glycolipid is the summation of head and tail volume:

$$\frac{M_{glycolipid}}{\rho_{glycolipid}} = \frac{M_{head}}{\rho_{head}} + \frac{M_{tail}}{\rho_{tail}} \quad (1)$$

where M_x and ρ_x stand for molar mass and specific density of compound/group x, respectively. Transformation of eq 1 leads to eq 2,

$$\frac{1}{\rho_{glycolipid}} = \frac{1}{\rho_{head}} + \left(\frac{1}{\rho_{tail}} - \frac{1}{\rho_{head}}\right)\frac{M_{tail}}{M_{glycolipid}} \quad (2)$$

which can be used to fit the inverse of glycolipid density ($1/\rho_{glycolipid}$) as a linear function of the molar mass fraction of the tail ($M_{tail}/M_{glycolipid}$). The intercept of the linear function (see Figures S28 and S29) yields the inverse of the specific density of the sugar headgroup, and the slope can be used to obtain the inverse of the specific density of the lipid. The resulting values for the specific densities of the head and tail groups for the two anomers and three temperatures are reported in Table S4. The differences in the head and tail densities between the anomers are very small (<0.6%), and we use linear fits (based on values for both anomers) to determine the specific density−temperature relations for the head and tail groups:

$$\rho_{head}(T) = 1.742\ \text{g cm}^{-3} - 0.00098\ \text{g cm}^{-3}\ \text{K}^{-1} \times T \quad (3)$$

$$\rho_{tail}(T) = 1.045\ \text{g cm}^{-3} - 0.00071\ \text{g cm}^{-3}\ \text{K}^{-1} \times T \quad (4)$$

At room temperature, eqs 3 and 4 yield values of 1.450 and 0.833 g cm^{-3}, respectively, for the specific densities of the sugar head and lipid tail groups that differ by 4% but in opposite direction from the values suggested by Nguan et al. In addition, the magnitude of the density−temperature coefficient is found here to be larger for the sugar headgroup than the lipid tail group, whereas the opposite is true for the values suggested by Nguan et al. Thus, the deviation between volume fractions based on the density values obtained by eqs. 3 and 4 and those suggested in the literature will increase with increasing temperature. The value of 1.450 g cm^{-3} for the sugar headgroup in the partially disordered lamellar phase also appears reasonable compared to the specific density of crystalline cellobiose of 1.560 g/cm^3.[31] On the other hand, the specific density values of 0.768 and 0.726 g cm^{-3} for the lipid tail group at 390 and 450 K, respectively, fall about 3% above those for liquid n-hexadecane at 45 MPa and the corresponding temperatures;[32] that is, reflecting the packing constraints of the partially disordered lamellar phase. We recommend the use of eqs 3 and 4 for the estimation of volume fractions for glycolipids.

MD Simulation of α-Cel−C_8C_4 and β-Cel−C_8C_4. MD simulations were conducted to study the phase behaviors of α-Cel−C_8C_4 and β-Cel−C_8C_4 at 390 K. To model the glycolipids, a combined force field is applied, where CHARMM all-atom potentials[33−36] and TraPPE united-atom potentials[37−39] are used to model the sugar head and the alkyl tail, respectively. The initial LAM configuration is constructed by inserting the glycolipids into an orthorhombic simulation cell using the PACKMOL package.[40] The simulation is then carried out using GROMACS 2019[41] with an isothermal−isobaric (NPT) ensemble, where the simulation box is allowed to fluctuate in three dimensions independently. The Berendsen thermostat with a time constant of 0.4 ps and Berendsen barostat with a time constant of 10 ps are used for temperature and

https://doi.org/10.1021/acs.biomac.3c01266
Biomacromolecules 2024, 25, 1291−1302

Scheme 1. Lewis Acid-Mediated Glycosylation Synthesis of Guerbet α- and β-Cellobiosides

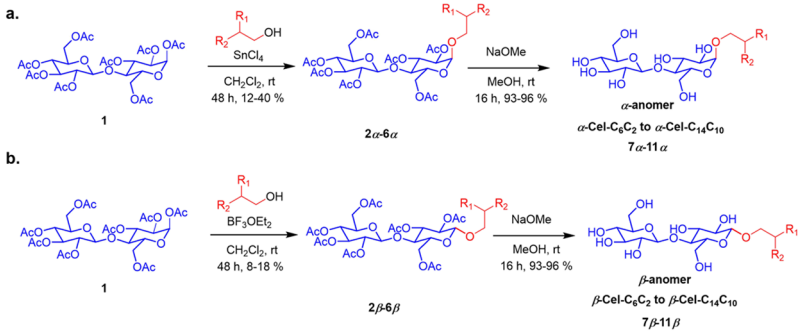

Compound number	R_1 ($C_{2m}H_{4m+1}$)	R_2 ($C_{2m+2}H_{4m+5}$)
α-Cel-C_6C_2 (**7α**), β-Cel-C_6C_2 (**7β**)	$m = 1$	$m = 1$
α-Cel-C_8C_4 (**8α**), β-Cel-C_8C_4 (**8β**)	$m = 2$	$m = 2$
α-Cel-$C_{10}C_6$ (**9α**), β-Cel-$C_{10}C_6$ (**9β**)	$m = 3$	$m = 3$
α-Cel-$C_{12}C_8$ (**10α**), β-Cel-$C_{12}C_8$ (**10β**)	$m = 4$	$m = 4$
α-Cel-$C_{14}C_{10}$ (**11α**), β-Cel-$C_{14}C_{10}$ (**11β**)	$m = 5$	$m = 5$

Table 1. Thermal and Structural Characterization of α- and β-cellobioside Thermotropic Liquid Crystals

	α-anomer		β-anomer	
guerbet cellobiosides	T_{ODT}[a] (°C)	lattice parameter (Å)[b]	T_{ODT}[a] (°C)	lattice parameter (Å)[b]
Cel−C_6C_2	125 (LAM → DIS)	31.7 (LAM)	163 (LAM → DIS)	32.1 (LAM)
Cel−C_8C_4	168 (LAM → DIS)	27.8 (LAM)	178 (LAM → DIS)	31.1 (LAM)
Cel−$C_{10}C_6$	174 (LAM → DIS)	30.5 (LAM)	179 (DG → DIS)	81.8 (DG)
Cel−$C_{12}C_8$	162 (DG → DIS)	81.4 (DG)	211 (HEX → DIS)	40.4 (HEX)
Cel−$C_{14}C_{10}$	187 (HEX → DIS)	85.6 (DG)	231 (HEX → DIS)	41.7 (HEX)

[a]T_{ODT} determined by DSC, and liquid crystal structure determined by SAXS (LAM = lamellae, DG = double gyroid, HEX = hexagonally packed cylinders, and DIS = disorder). [b]All the lattice parameters were obtained from SAXS analyses at 115 °C except for the β-C_6C_2, for which the value was obtained at 145 °C where it started forming the LC phase. All the corresponding phase is noted in parentheses.

pressure coupling.[42] Both systems are allowed to equilibrate for over 1.8 μs, after which a 200 ns simulation was performed for production run and used for analysis. The resulting data are averaged over the 200 ns time window.

RESULTS AND DISCUSSION

Guerbet cellobiosides were synthesized by Lewis acid-mediated glycosylation reactions of peracetylated cellobiose with Guerbet-type alcohols of the type $HOCH_2CHR_1R_2$ (R_1 = $C_{2m+2}H_{4m+5}$ and R_2 = $C_{2m}H_{4m+1}$, m = 1−5).[43] Reactions mediated by BF_3•Et_2O in CH_2Cl_2 (Scheme 1a) yielded primarily 1:2 mixtures of α and β glycolipids per literature precedents.[25] Silica gel chromatography enabled the purification and isolation of the pure β-anomers from these mixtures in modest yields. On the other hand, the α-anomers could not be easily isolated in sufficiently high yields and purities.[44] Per a slight modification of an earlier report,[27,45] access to α-cellobioside anomers instead relied on glycosylations in the presence of $SnCl_4$ (Scheme 1b). This procedure typically yielded 3:1 mixtures of the α- and β-anomers, from which the α-anomer could be chromatographically separated in high purity. Detailed synthesis and purification procedures are given in the Supporting Information, along with associated ^{1}H and ^{13}C NMR spectra of the homologous cellobioside series (see Figures S1−S10). Given our interest in the thermotropic phase behaviors of these molecules in the absence of H_2O, all compounds were extensively lyophilized prior to storage in a glovebox under nitrogen. Sample purity and the removal of trace water were confirmed by elemental analysis (see Supporting Information Section VIII). These compounds are hereafter referred to as x-Cel−C_yC_{y-4}, where x refers to either α- or β-anomer stereochemistry, and even parity y = 6−14 refers to the longer alkyl chain length of the Guerbet alcohol.

The thermotropic phase transitions of these Guerbet cellobiosides were initially investigated by DSC, in order to identify the temperature window over which thermotropic liquid crystalline self-assembly occurs. DSC thermograms obtained using a heating rate of 5 °C/min in all cases reveal weak, steplike discontinuities indicative of a molecular mobility transition in the range 55 ≤ T ≤ 88 °C during the first heating (see Figure S11 and Table S1). No systematic trends in these transition temperatures could be discerned as a function of the Guerbet alkyl tail length. Related observations reported for both Guerbet maltosides[46] and monoalkyl glucosides[47] (where 6 ≤ n ≤ 12) were ascribed to glass transition temperatures (T_g) of these molecular amphiphiles. In the case of dodecyl maltoside and dodecyl maltotrioside, this apparent T_g crucially depends on the oligosaccharide headgroup structure rather than that of the tails.[48] We further note that the location of the T_g observed here is in proximity to the cellobiose T_g = 62 °C,[49] with modest variations that likely arise from molecular packings induced by the presence of specific Guerbet tails.

In contrast to straight-chain n-alkyl cellobiosides, melting transitions were only sometimes observed by DSC for the

https://doi.org/10.1021/acs.biomac.3c01266
Biomacromolecules 2024, 25, 1291−1302

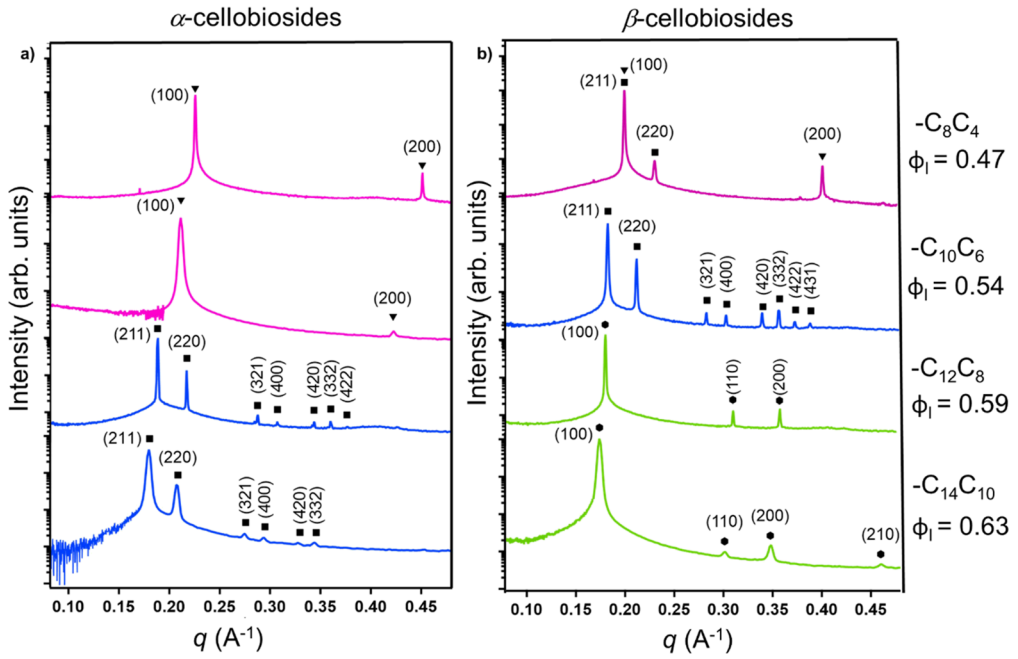

Figure 1. Azimuthally integrated synchrotron SAXS intensity profiles for α-cellobiosides and β-cellobiosides at 115 °C with different Guerbet chain lengths, which are vertically shifted for clarity. On each trace, the filled triangle, square, and hexagonal markers indicate calculated peak positions associated with LAM, DG, and HEX phases, respectively.

homologous series of Guerbet cellobiosides with the exception of those with the largest ($-C_{14}C_{10}$) tail (Figure S11a,b). These findings are consistent with prior reports on a series of β-Guerbet maltosides.[46] Variable temperature POM with ±5 °C degree temperature resolution was instead used to detect the melting transitions, as in prior work on dodecyl and octadecyl cellobiosides.[25] These POM and DSC experiments establish that the cellobiosides form LC phases when $T \geq 85$ °C for $-C_8C_4$ or longer branched alkyl tails. Accordingly, structures are denoted as CRYS when $T < 85$ °C.

For each Guerbet cellobioside, we also observe a sharp, high-temperature melting endotherm of modest size that we assign to the thermotropic LC clearing temperature, also called the order-to-disorder transition (ODT) temperature (T_{ODT}; see Figure S11). The value of T_{ODT} increases monotonically with increasing alkyl tail length in each of the α- and β-anomer series (see Table 1 for values), in a manner reminiscent of structurally related Guerbet maltosides.[46] Due to the high stereochemical purity of the compounds reported here, these DSC data clearly demonstrate that the β-anomers exhibit higher T_{ODT} values than the stereoisomeric α-anomers. A similar trend has been previously reported in lamellae-forming (smectic A) monosaccharide-based glycolipids. In the latter case, the relatively higher T_{ODT} values for the β-anomers were ascribed to stronger hydrogen bonding interactions between the glycolipid headgroups within each microphase-separated lamella.[50−52]

Variable-temperature SAXS measurements demonstrate that anomeric cellobiosides α-Cel$-C_6C_2$ and β-Cel$-C_6C_2$ with the shortest Guerbet tail form thermotropic lamellar phases, indicated by the presence of SAXS peaks corresponding to the (100), (200) reflections (Figures S12). The lamellar d-spacing for the β-anomer LC is slightly larger than that for the α-anomer (Tables 1, S2 and Figure S12).

SAXS analyses of Guerbet cellobiosides with longer alkyl tail lengths at 115 °C reveal how the thermotropic phase behaviors of these anomeric analogues depend on the carbon tail length (Figure 1). α-Cel$-C_8C_4$ and $-C_{10}C_6$ assemble into thermotropic lamellar (LAM) phases with peaks located at $(q/q^*)^2 = 1, 4$, and 9 with d-spacings that increase with tail length (Figures 1a, S13, and S14). However, lengthening the tail to $-C_{12}C_8$ or $-C_{14}C_{10}$ drives an order-to-order transition (OOT) to a new phase (Figure 1a). This new LC phase exhibits a unique scattering signature with characteristic peaks located at $(q/q^*)^2 = 6, 8, 14, 16, 20, 22$, etc. that correspond to the (211), (220), (321), (400), (420), and (332) reflections of a thermotropic DG phase with $Ia\bar{3}d$ space group symmetry (Figures S15 and S16). The unit cell parameters for these DG phases increase from 81.4 to 85.6 Å upon increasing the Guerbet tail length (see the lattice constants given in Table 1). In most cases, the observed phases exhibit isotropic ring patterns that suggest the formation of self-assembled structures with modest grain sizes; however, the highly textured ("spotty") SAXS patterns for α-Cel$-C_{12}C_8$ suggest the strong propensity for this compound to order into a DG phase with exceptional long-range-translational order (Figure S17g).

On the other hand, β-cellobioside self-assembly at 115 °C results in the isothermal phase sequence LAM + DG → DG → HEX with increasing tail length (Figure 1b), where HEX refers to hexagonally packed cylinders phases with SAXS peaks located at $(q/q^*)^2 = 1, 3, 4, 7$, etc. with $P6mm$ symmetry. Based on the variable temperature melt densities of the Guerbet tails and cellobiose headgroups obtained from MD simulations (see Supporting Information Section VII), the hydrophobic lipid tail volume fraction is $\phi_l \geq 0.54$ for cellobiosides with alkyl tails longer than $-C_{10}C_6$. This volume composition suggests that the observed DG phase comprises cables of saccharide groups in a matrix of hydrocarbon tails. This morphological assignment was confirmed by POM measurements in which alkyl tail-soluble octane was added to β-Cel$-C_{10}C_6$ at 115 °C, which drove a DG → HEX phase transition, as is expected upon swelling the hydrocarbon matrix

https://doi.org/10.1021/acs.biomac.3c01266
Biomacromolecules 2024, 25, 1291−1302

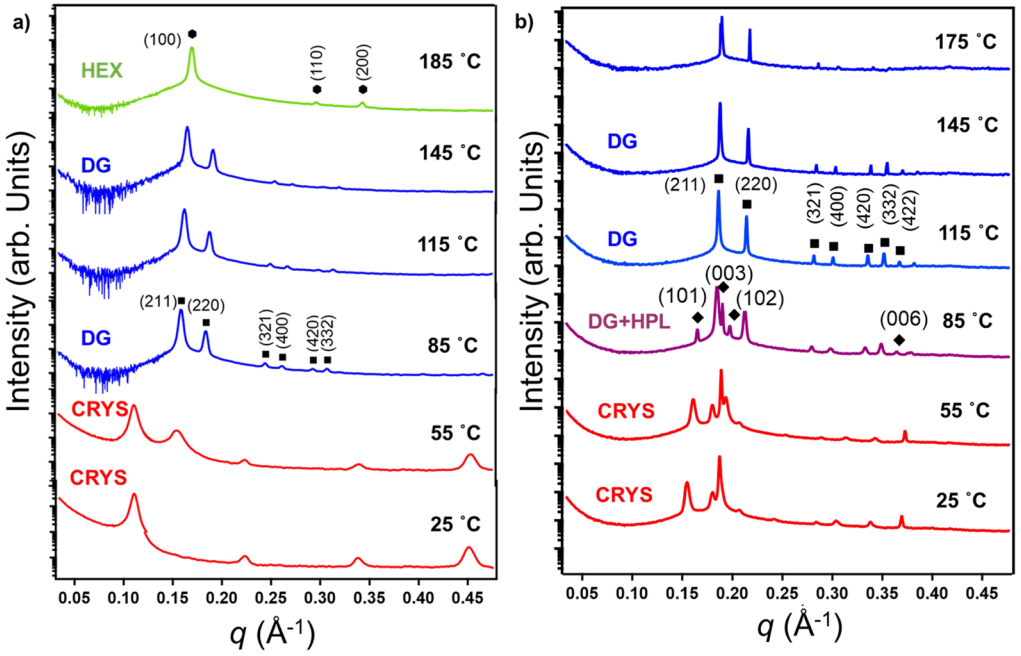

Figure 2. Temperature-dependent synchrotron SAXS patterns obtained for (a) α-Cel−$C_{14}C_{10}$ and (b) β-Cel−$C_{10}C_6$, with intensity profiles vertically offset for clarity. The characteristic Bragg reflections of LAM, DG, HEX, and HPL phases were indicated by filled triangle, square, hexagonal, and diamond symbols, respectively.

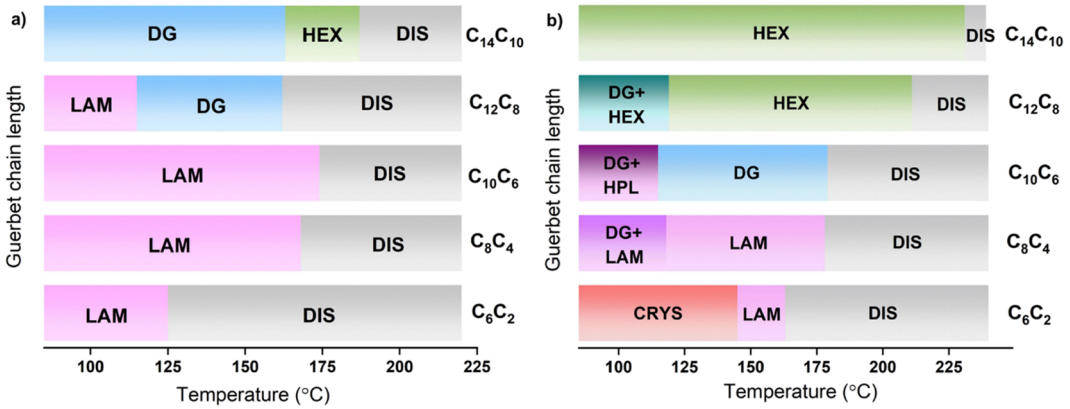

Figure 3. Phase behavior observed on heating of dry (a) α-cellobiosides and (b) β-cellobiosides within the temperature range of 25−235 °C at a ramp rate of 10 °C/min. DIS and CRYS represent the disordered and crystallized phases, respectively.

domain (see Figure S19j,k). Note that the $-C_8C_4$ tail length at which we observe the OOT from LAM to DG depends sensitively on the anomeric stereochemistry.

Temperature-dependent SAXS measurements revealed that the thermotropic DG phases formed by these cellobiosides exhibit large temperature stability windows (Figure 2), which rival or even exceed those previously reported for glycolipids.[24,46,52] For example, the pure DG phase of β-Cel−$C_{10}C_6$ persists over a ΔT = 64 °C temperature window spanning 115−179 °C (Figure 2b). Note that DSC and POM analyses reveal that heating this sample to $T \geq 115$ °C does not drive any OOTs prior to reaching T_{ODT} = 179 °C. At lower temperatures, this DG apparently coexists with another morphology that we assign as a hexagonally perforated layer (HPL) phase with *R3m* space group symmetry, based on the appearance of (101), (003), (102), and (006) reflections with unit cell parameters a = 47.4 Å and c = 98.2 Å. Although the calculated c/a = 2.07 is smaller than that observed in high molar mass block linear diblock copolymers,[53] the occurrence of HPL in close proximity to a DG phase is well-precedented[54] as both phases exhibit negative Gaussian curvature interfaces. Upon heating this sample above T_{ODT} and cooling it back to 25 °C, we observed the formation of a stable DG phase with a "spotty" SAXS pattern consistent with the formation of large, ordered domains (Figure S20a). The irreversible reversion of the high-temperature DG phase to the low-temperature phases observed on sample heating on experimental time scales, which is similar to the case in block copolymers,[55,56] likely stems from the significant energetic penalties for molecular reconfiguration required for such phase transformations. Finally, SAXS analyses of β-Cel−$C_{12}C_8$ and $-C_{14}C_{10}$ primarily form ordered HEX phases below T_{ODT} in a manner consistent with the above volume-filling arguments.

In the case of α-Cel−$C_{14}C_{10}$, temperature-dependent SAXS reveals the stability of the DG phase between 85 and 145 °C. Upon careful inspection of the DSC trace for this sample (Figure S11), we note the presence of an endothermic peak that marks the phase transition at 163 °C from DG to the high-

https://doi.org/10.1021/acs.biomac.3c01266
Biomacromolecules 2024, 25, 1291−1302

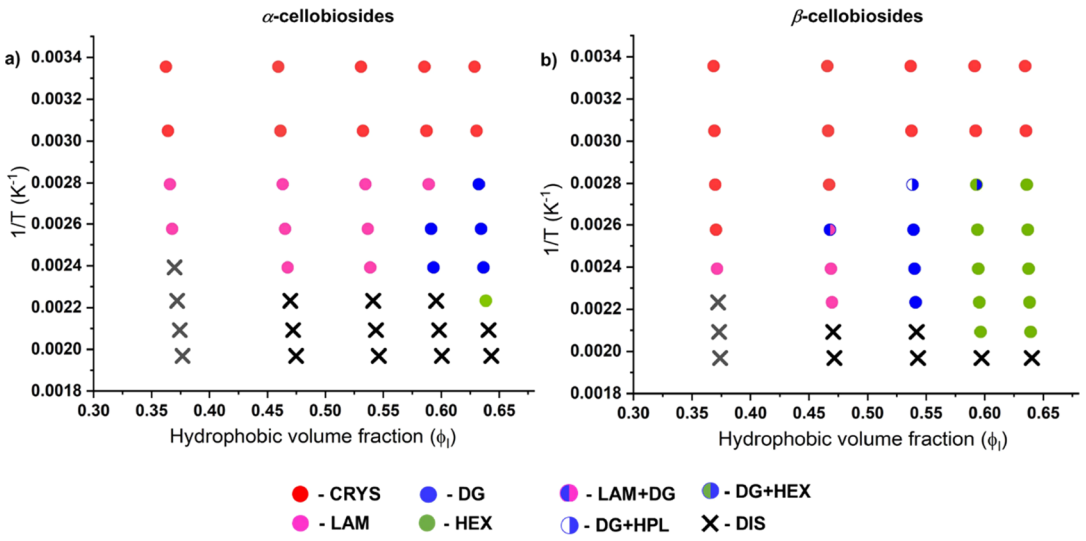

Figure 4. $1/T$ versus ϕ_l morphology diagram for (a) α-Guerbet cellobiosides and (b) β-Guerbet cellobiosides, demonstrating differences in their thermotropic phase progressions with increasing ϕ_l, where crystalline amphiphile is denoted CRYS (red, circles), LAM (pink, circles), DG (blue, circles), HEX (green, circles), and DIS (X) refer to the observed LC phases.

temperature HEX phase observed by SAXS (Figure 2a). Thus, the thermal stability window for the pure DG phase of α-Cel−$C_{14}C_{10}$ is ΔT = 76 °C, which is even wider than that of β-Cel−$C_{10}C_6$ and α-Cel−$C_{12}C_8$ (ΔT = 64 and 47 °C from Figures S11, S14, and S15). The formation of a high-temperature HEX phase likely arises in the volume filled by the lipidic tail due to temperature-dependent increases in its conformational degrees of freedom. We further note that the high-temperature HEX phase of α-Cel−$C_{14}C_{10}$ exhibits a smaller d-spacing than that of the β-anomer, similar to the aforementioned anomer-dependent LAM d-spacing trends (Tables S2 and S3). Representative temperature-dependent SAXS profiles for all of the Guerbet glycolipids reported here are given in Figures S12−S16.

These SAXS data for structurally homologous α- and β-cellobiosides clearly highlight the key role of the anomeric configuration in dictating their thermotropic self-assembly behaviors. Figure 3 summarizes the tail length- and temperature-dependent phase behaviors of the cellobiosides for T = 25−235 °C, based on DSC, variable temperature SAXS and POM experiments. As the glycolipid chain length increases, both anomers form nonlamellar phases. However, the critical chain length at which this transition occurs is smaller for the β-anomers as compared to α. Zahid et al. previously noted the analogous role of anomeric stereochemistry in governing LC phase selection in glucopyranoside and galactopyranoside glycolipids bearing $-C_{10}C_6$ Guerbet-type tails.[24] In that work, they observed that the α-anomer generally formed flatter curvature interfaces than the β-anomer (e.g., α forms LAM while β forms DG + HEX coexistence).

In order to better visualize how variations in hydrophobic volume (tail length) and anomeric stereochemistry direct temperature-dependent Guerbet cellobioside self-assembly, we recast the data in Figure 3 in the form of a $(1/T)$ versus ϕ_l morphology diagram as in Figure 4. The choice of the ordinate as $(1/T)$ is inspired by analogies between LC self-assembly and theoretical[57,58] and experimental[59,60] studies of block copolymer microphase separation.[61,62] In the latter systems, increasing the temperature results in a decrease in the energetic repulsions between chemically dissimilar segments quantified by the effective interaction parameter that follows the empirical form $\chi(T) = (A/T) + B$.[63]

These morphology diagrams reveal a clear shift in the DG phase windows toward higher φ_l for the α-anomers (ϕ_l = 0.6−0.65, Figure 4a) in comparison to the β-anomers (ϕ_l = 0.48−0.6, Figure 4b). Notably, the composition window width over which pure DG phases form is modestly wider for the α-anomers than for the β-anomers. As noted above, the thermal stability window (best reflected in Figure 3) is also comparatively wider for the α-anomers. Finally, these morphology diagrams also indicate that the ODT transition shifts to lower $(1/T)$ values or lower interfacial tensions on going from the α to the β stereochemistry. In the language of thermodynamically-driven block copolymer self-assembly, the hydrophobic and hydrophilic segments of the α-anomers act as if they are more weakly segregated than in the β case. These changes altogether imply significant differences in the molecular packings between the anomers at the same ϕ_l, with different tendencies to segregate the chemically dissimilar segments.

To better understand the anomer-dependent molecular packings of these Guerbet glycolipids, LAM-forming cellobiosides were examined using atomistic molecular simulations. Systems are allowed to equilibrate for 1.8 μs. The last 200 ns trajectories from 1.8−2.0 μs were used for analysis, and the results were averaged over the time window. More simulation details are included in the Supporting Information. As noted above, β-cellobiosides always exhibit larger LAM and HEX phase d-spacings than the α-anomers (Tables 1 and S2). MD simulations on LAM-forming α-Cel−C_8C_4 and β-Cel−C_8C_4 at 390 K capture this experimental behavior well, yielding significantly different d-spacings (see Supporting Information Section XVII). The MD simulation values are in close quantitative agreement with experiments (<2% difference), with d_{MD}= 27.3 Å versus d_{exp}= 27.8 Å for the α-anomer and d_{MD} = 31.4 Å versus d_{exp} = 31.1 Å for the β-anomer from the calculated static structure factor (Figure S21). A similar trend has been reported previously for the different anomers of alkyl glucosides.[64−68] These prior studies hinted that the specific stereochemistry led to a kinked or "boomerang-shaped"

https://doi.org/10.1021/acs.biomac.3c01266
Biomacromolecules 2024, 25, 1291−1302

molecule for α-anomers that shortens the molecules (and thus their LAM d-spacings) relative to the corresponding β-anomers, which instead adopt a comparatively linear structure.[69]

The preferentially observed molecular conformations for each Cel−C_8C_4 anomer and other analyses from MD simulations are consistent with a shorter, bent shape for the α-anomers (Figure 5). Here, the glycolipid plane is defined as

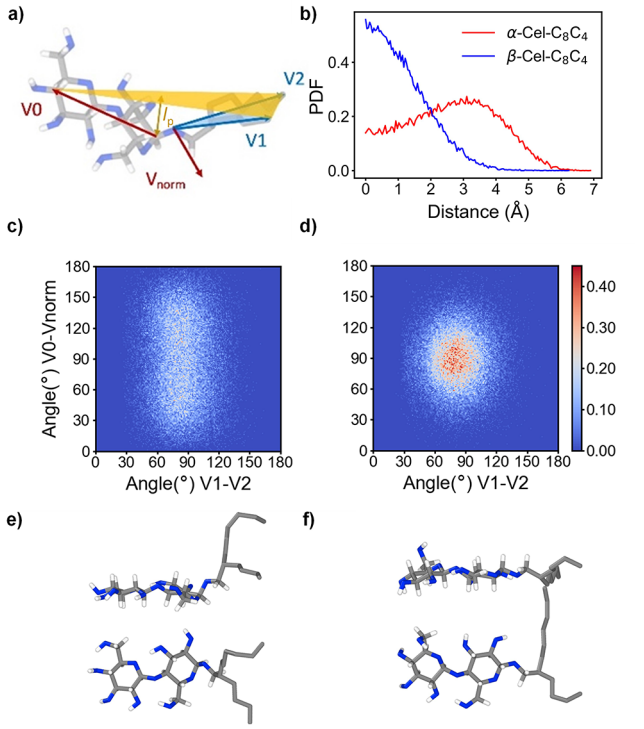

Figure 5. Molecular conformations of Cel−C_8C_4 at 390 K (LAM) from MD simulations. (a) Sketch of the plane formed by the distal carbon atoms of the sugar and tail groups (yellow, "glycolipid plane") and by the ether linker and tail ends (blue "tail plane"). (b) Probability distribution of the distance l_p between the C1 atom and the glycolipid plane for α- (red) and β-(blue) anomers. (c, d) Heat maps of the tail splay angle (V_1−V_2) and angle between the long axis of the headgroup and the normal to the tail plane (V_0−V_{norm}) for (c) α- and (d) β-anomers. The probability in the color bar is scaled by 1000. (e, f) High probability conformations of (e) α- and (f) β-Cel−C_8C_4.

that formed by the distal carbon atoms of the sugar and tail groups (yellow plane; Figure 5a). Probability distributions (Figure 5b) of the distance, l_p, between the C1 atom proximal to the glycosidic linker to the tail group and this plane indicate that the β-anomer prefers more planar conformations, with l_p < 1 Å and a relatively narrow distribution. In contrast, the α-anomer retains a broad range of conformations, most of which are boomerang-shaped. The most probable α-anomer conformations have 3 Å ≤ l_p ≤ 4 Å, and a strongly bent shape that is only very sparsely populated for the β-anomer.

Heat maps depicting the conformational populations in a 2D space defined by the tail splay angle (V_1 to V_2) and the angle between the cellobioside headgroup and the normal to the tailplane (V_{norm} to V_0) similarly suggest that α-anomers adopt a wider range of molecular conformations in the LAM phase than the β-anomers (Figure 5c versus d). As expected based on the semirigid nature of the short tails, the distribution of tail splay angles is similar for both anomers with a preference for (80 ± 20)°. However, for β-anomers, the headgroup orientation is preferentially coplanar with tail groups as indicated by the strong preference for the V_0−V_{norm} angle being near 90° (red region, Figure 5d). In contrast, the observed conformations for the α-anomer are clustered around two broad lobes (Figure 5c), and V_0−V_{norm} angles from 20 to 160° are well populated. The bent shape of α-Cel−C_8C_4 relative to β-Cel−C_8C_4 is also well-illustrated by their typical conformations depicted in Figure 5e,f, respectively. The distributions of distances between distal carbon atoms of the sugar and tail groups (Figure S22) also indicate that both average head-to-tail distances are shorter for the α-anomer. Another important feature of the broad range of conformations adopted by the α-anomer is that one of the tail groups can fold back over the sugar headgroup (Figure S23), whereas such conformations are not observed for the β-anomer. This structural analysis indicates that α-anomers adopt a very broad range of conformations upon LC packing compared to the corresponding β-anomers, which prefer a narrow range of conformations. Thus, unlike the β-anomers, the α-anomers are not only "boomerang-shaped", but packing frustration imparted by their irregular shape leads them to not adopt specific molecular conformations.

To gain deeper experimental insights into the molecular packings in these thermotropic phases, POM was conducted on the LAM-forming cellobiosides with −C_6C_2 and −C_8C_4 tails to determine whether the various anomers assemble into LCs with net in-plane orientation. POM images obtained upon both heating and cooling the α- and β-anomers of Cel−C_8C_4 and Cel−C_6C_2 exhibit focal conic textures, indicative of lamellar smectic A (SmA) assemblies in all cases (Figures 6a,b

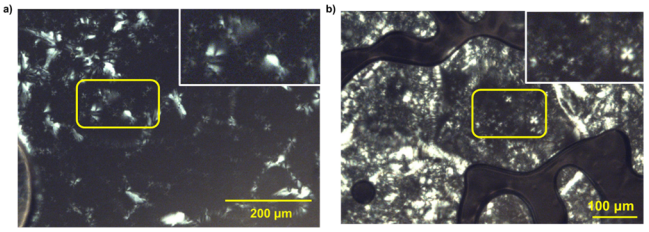

Figure 6. POM images taken while heating (a) α-Cel−C_8C_4 at 10 °C/min showing a focal conic texture representative of a SmA phase, and (b) β-Cel−C_8C_4 while cooling at 10 °C/min again showing similar a SmA focal conic texture (inset shows a zoomed in portion marked within yellow box).

and S19). Thus, the boomerang shape-filling profiles of the α-anomers are not sufficiently stiff to enforce the LC orientational order within the lamellae. The apparent SmA packing in the α-anomers may be rationalized by local density maps from MD simulations (Figure S24a), which indicate significant overlap between the cellobiose headgroups and Guerbet tails in both the "tail" region (middle of the bilayer) and "head" region (0.5d from bilayer center). This head and tail group overlap is absent in the more planar β-anomers that can more easily pack into LAM phases (Figure S24b), consistent with shape-dependent packing differences observed in n-dodecyl β-disaccharides with varied sugar head groups.[70] These local density maps also suggest that the α-anomer shape is sufficiently irregular to prevent packing into either oriented smectic C (SmC) or well-ordered yet nonoverlapping SmA

https://doi.org/10.1021/acs.biomac.3c01266
Biomacromolecules 2024, 25, 1291−1302

phases. Furthermore, a high degree of overlap between the heads and tails is required for α-anomer packing into bilayers.

In SmA-forming glycolipids, the higher T_{ODT} values of the β-anomers relative to those of their α-homologues (Table 1) imply greater cohesion between the oligosaccharide and hydrocarbon domains. The stronger segregation of the β-anomers (Figure 4) suggests anomer-configuration-dependent differences in the cohesive energy densities of the two domains. Since the lipid tails must pack with near constant density to maximize van der Waals cohesion, the key differences in intermolecular cohesion must arise from variations in the hydrogen bonding patterns in the polar sugar domains. Prior reports have ascribed stereochemically driven differences in T_{ODT} for anomeric glycolipids to either a greater number or stronger H-bonds between headgroups within the same layer (intralayer) for β-anomers; interlayer H-bonds are thought to influence T_{ODT} less significantly.[50−52] If true, this kind of H-bonding pattern in the β-anomers suggests a more constrained headgroup arrangement and tighter molecular packing.[69,71]

Indeed, the MD simulations show a flatter molecular shape with minimal headgroup and tail overlap in the β-anomers (Figure S24b) that results in their significantly higher headgroup packing density than in the α-anomers (Figure S24a). Consequently, the overall density of the headgroup region is slightly higher in the β- relative to the α-anomers (Figure S25). These findings concur with prior molecular simulations[72,73] of the lamellar packings of LCs of *n*-alkyglycoside anomers. Heat maps of the H-bonding between sugar headgroups for each anomer also support the higher T_{ODT} values and a more constrained headgroup environment for the β-anomers. These maps further reveal a similar number of interlayer H-bonds (Figure S26a,b), yet a comparatively larger number of intralayer H-bonds for the β- versus the α-anomers (Figure S26c,d). As expected, an increase in the number of intralayer H-bonds between hydroxyl groups near the alkyl tail is observed for both anomers compared with the interlayer case. The β-anomers exhibit a more ordered alignment, with a high probability of H-bond formation between C3′ and C6′, C2 and C6 hydroxyl groups. Conversely, the probability of H-bond formation for the α-anomers is more uniformly distributed.

Consistent with limited overlap between opposing β-anomer headgroups, the majority of the interlayer hydrogen bonds occur between opposing hydroxyl groups in positions far from the alkyl tails, i.e., off of the C3′, C4′, and C6′ atoms (Figure S26b). The highest probability H-bonds form between pairs of opposing C3′ or C4′ hydroxyls followed by H-bonds between opposing C3′ and C4′ hydroxyl groups, which reflect the regular, well-ordered packing. H-bonds between these same three hydroxyl groups are also the most probable for the α-anomers with a generally lower frequency. More specifically, H-bonds between opposing C3′ and C4′ −OH groups are instead most probable followed by those between opposing C4′ hydroxyls (Figure S26a). H-bonds between all other combinations of C3′, C4′, and C6′ hydroxyls form less often but with similar probabilities, reflecting increased headgroup overlap and less regular packing for the α-anomers. A higher number of H-bonds between specific hydroxyl groups is observed only in one instance for the α-anomers: the C4' and C6' hydroxyls. This unusual H-bonding pattern suggests that the α-anomer head groups tilt significantly from the bilayer normal to bring these hydroxyl groups in close proximity, consistent with simulations of thermotropic maltosides and cellobiosides with linear *n*-alkyl tails.[70] The distribution of angles between the sugar headgroup and bilayer normal is consistent with this hypothesis (Figure S27), where α-anomers adopt a broad distribution of tilt angles centered around a most probable tilt angle of ∼44° versus ∼34° for β-anomers, albeit with a broader angular distribution for the α-anomers.

In the α-anomers, the wide range of molecular conformations, tilt angles, and higher degree of overlap between the cellobiose headgroup and Guerbet tails upon assembly arise from the packing frustration imparted by their shape-filling character that destabilizes constant mean curvature packings.[74,75] Detailed analyses of simulated bilayers reveal that those formed by the β-anomer maintain a zero-mean curvature planar topology, while the α-anomers form a noticeably wavy bilayer (Figure S24c). The latter structure is also apparently more susceptible to wrinkling fluctuations, as time-dependent simulation trajectories of over 200 ns demonstrate its bending. These observations provocatively suggest that the α-anomer bilayer exhibits a lower bending modulus than the stiffer β-anomer analogue. Notably, the degree of headgroup and tail overlap increases in areas of nonzero curvature, with an increasing fraction of sugar headgroups found in the bilayer center. One means of relieving these steric interactions is to transition into a nonlamellar morphology. In this vein, large amplitude undulations in LAM are often observed proximal to temperature-dependent OOTs into HPL and DG phases,[76−79] as in the observed LAM → DG transition at elevated temperatures for α-Cel−$C_{12}C_8$. The greater headgroup tilt relative to the bilayer normal noted for the α-anomers may additionally relieve packing frustration associated with negative Gaussian ("saddle splay") curvature interface formation in the DG, in a manner akin to lipid tilting to relieve saddle packing frustration in lipid membrane fusion and buckling events.[80,81]

The wider range of possible molecular conformations, the increased overlap between the head and tail groups on packing, reduced numbers of H-bonds, and the lower bilayer bending modulus in the α-anomers all suggest their ability to more easily accommodate increasing degrees of chain splay associated with longer lipidic tails. Consequently, the transient bilayer wrinkling fluctuations may occur for the α-Cel−C_8C_4, however, the phase transition to a DG is delayed until the alkyl tail is elongated to −$C_{12}C_8$. On the other hand, steric interactions incurred by the lipid tails in the more tightly packed β-anomer likely trigger the LAM → DG transition at shorter tail lengths. The wider thermal stability window (ΔT) for the DG obtained of α-Cel−$C_{14}C_{10}$ compared to β-Cel−$C_{10}C_6$ likely stems from the fact that the α-anomers can more readily accommodate geometric fluctuations by virtue of their less dense, anisotropic packings compared to the β-isomers. Collectively, these results highlight how the anomeric configuration in disaccharide-based Guerbet glycolipids guides their self-assembled phase selection and ability to form remarkably thermally stable DG phases.

CONCLUSIONS

Complementary experimental and MD studies of the thermotropic liquid crystalline behaviors of anomerically pure Guerbet cellobiosides with varied alkyl tail lengths have revealed how stereochemistry influences amphiphile shape-filling and supramolecular self-assembly into lamellar, hexagonal, and DG network phases. The stereochemical configuration of the anomeric linkage between the cellobiose

https://doi.org/10.1021/acs.biomac.3c01266
Biomacromolecules 2024, 25, 1291−1302

headgroup and the branched alkyl tail specifically influences the preferred spatial periodicities and thermal stabilities of these assemblies. Experimentally, we observed that the α-anomers assemble into DG phases over wider thermal windows and with a wider range of lipidic tail lengths than their corresponding β-anomers. Anomer-dependent differences in Guerbet cellobioside self-assembly likely arise from stereochemically driven changes in the preferred molecular conformations that maximize noncovalent intermolecular cohesion within these molecular assemblies. MD simulation illustrates that β-anomers display primarily planar conformations adopting more constrained, high-density intermolecular packings within relatively stiff bilayers, with no substantial interdigitation of the amphiphile heads or tails. However, the α-anomers exhibit kinked or boomerang-like shapes with a large number of possible alkyl tail configurations, which lead to less dense sugar headgroup packings with substantial head and tail interdigitation in less stiff bilayers that are prone to wrinkling fluctuations in simulations. Thus, the latter amphiphiles are better able to support the formation of stable DG phases over exceptionally wide thermal windows. These findings suggest that the design of anisotropic shape-filling molecular amphiphiles may generally destabilize the self-assembly of the zero curvature lamellar phase in favor of 3D network assemblies that crucially require the formation of saddle curvature interfaces.

■ ASSOCIATED CONTENT

Supporting Information

The Supporting Information is available free of charge at https://pubs.acs.org/doi/10.1021/acs.biomac.3c01266.

Glycolipid synthesis protocols, ^{1}H and ^{13}C NMR spectra, DSC and temperature-dependent SAXS intensity profile and tabulated lattice constants, POM images, and detailed description and analyses of MD simulation results (PDF)

■ AUTHOR INFORMATION

Corresponding Authors

J. Ilja Siepmann − *Department of Chemistry, University of Minnesota Twin Cities, Minneapolis, Minnesota 55455, United States;* orcid.org/0000-0003-2534-4507; Email: siepmann@umn.edu

Mahesh K. Mahanthappa − *Department of Chemical Engineering and Materials Science, University of Minnesota Twin Cities, Minneapolis, Minnesota 55455, United States;* orcid.org/0000-0002-9871-804X; Email: maheshkm@umn.edu

Michelle A. Calabrese − *Department of Chemical Engineering and Materials Science, University of Minnesota Twin Cities, Minneapolis, Minnesota 55455, United States;* orcid.org/0000-0003-4577-6999; Email: mcalab@umn.edu

Theresa M. Reineke − *Department of Chemistry, University of Minnesota Twin Cities, Minneapolis, Minnesota 55455, United States;* orcid.org/0000-0001-7020-3450; Email: treineke@umn.edu

Authors

Soumi Das − *Department of Chemistry, University of Minnesota Twin Cities, Minneapolis, Minnesota 55455, United States*

Caini Zheng − *Department of Chemistry, University of Minnesota Twin Cities, Minneapolis, Minnesota 55455, United States*

Timothy P. Lodge − *Department of Chemistry, University of Minnesota Twin Cities, Minneapolis, Minnesota 55455, United States; Department of Chemical Engineering and Materials Science, University of Minnesota Twin Cities, Minneapolis, Minnesota 55455, United States;* orcid.org/0000-0001-5916-8834

Complete contact information is available at: https://pubs.acs.org/10.1021/acs.biomac.3c01266

Notes

The authors declare no competing financial interest.

■ ACKNOWLEDGMENTS

This work was supported primarily by the U.S. National Science Foundation through the University of Minnesota MRSEC under Award Number DMR-2011401. This research used resources of the Advanced Photon Source, a U.S. Department of Energy (DOE) Office of Science User Facility, operated for the DOE Office of Science by Argonne National Laboratory under Contract No. DE-AC02-06CH11357. SAXS experiments were carried out at Sector 5 and Sector 12 of the Advanced Photon Source. The Sector 5 DuPont-Northwestern-Dow Collaborative Access Team (DND-CAT) was supported by E.I. DuPont de Nemours & Co., the Dow Chemical Company, and Northwestern University. The authors also acknowledge the Minnesota Supercomputing Institute (MSI) at the University of Minnesota for providing resources that contributed to the research results reported within this paper.

■ REFERENCES

(1) Werner, J.; Rodríguez-Calero, G.; Abruña, H.; Wiesner, U. Block copolymer derived 3-D interpenetrating multifunctional gyroidal nanohybrids for electrical energy storage. *Energy Environ. Sci.* **2018**, *11* (5), 1261−1270.

(2) Feng, X.; Kawabata, K.; Kaufman, G.; Elimelech, M.; Osuji, C. O. Highly selective vertically aligned nanopores in sustainably derived polymer membranes by molecular templating. *ACS Nano* **2017**, *11* (4), 3911−3921.

(3) Caffrey, M.; Li, D.; Dukkipati, A. Membrane protein structure determination using crystallography and lipidic mesophases: recent advances and successes. *Biochemistry* **2012**, *51* (32), 6266−6288.

(4) Caffrey, M. Crystallizing membrane proteins for structure determination: use of lipidic mesophases. *Annu. Rev. Biophys.* **2009**, *38*, 29−51.

(5) Mezzenga, R.; Seddon, J. M.; Drummond, C. J.; Boyd, B. J.; Schröder-Turk, G. E.; Sagalowicz, L. Nature-inspired design and application of lipidic lyotropic liquid crystals. *Adv. Mater.* **2019**, *31* (35), No. 1900818.

(6) Zheng, L.; Bandara, S. R.; Tan, Z.; Leal, C. Lipid nanoparticle topology regulates endosomal escape and delivery of RNA to the cytoplasm. *Proc. Natl. Acad. Sci. U. S. A.* **2023**, *120* (27), No. e2301067120.

(7) Uchida, J.; Soberats, B.; Gupta, M.; Kato, T. Advanced functional liquid crystals. *Adv. Mater.* **2022**, *34* (23), No. 2109063.

(8) Tschierske, C. Development of structural complexity by liquid-crystal self-assembly. *Angew. Chem., Int. Ed. Engl.* **2013**, *52* (34), 8828−8878.

(9) Poppe, S.; Cheng, X.; Chen, C.; Zeng, X.; Zhang, R.-B.; Liu, F.; Ungar, G.; Tschierske, C. Liquid organic frameworks: The single-network "Plumber's Nightmare" bicontinuous vubic liquid crystal. *J. Am. Chem. Soc.* **2020**, *142* (7), 3296−3300.

(10) Cai, X.; Hauche, S.; Poppe, S.; Cao, Y.; Zhang, L.; Huang, C.; Tschierske, C.; Liu, F. Network phases with multiple-junction geometries at the gyroid−diamond transition. *J. Am. Chem. Soc.* **2023**, *145* (2), 1000−1010.
(11) Ichikawa, T.; Yoshio, M.; Hamasaki, A.; Taguchi, S.; Liu, F.; Zeng, X.-B.; Ungar, G.; Ohno, H.; Kato, T. Induction of thermotropic bicontinuous cubic phases in liquid-crystalline ammonium and phosphonium salts. *J. Am. Chem. Soc.* **2012**, *134* (5), 2634−2643.
(12) Alam, M. A.; Motoyanagi, J.; Yamamoto, Y.; Fukushima, T.; Kim, J.; Kato, K.; Takata, M.; Saeki, A.; Seki, S.; Tagawa, S. "Bicontinuous cubic" liquid crystalline materials from discotic molecules: a special effect of paraffinic side chains with ionic liquid pendants. *J. Am. Chem. Soc.* **2009**, *131* (49), 17722−17723.
(13) Zeng, X.; Prehm, M.; Ungar, G.; Tschierske, C.; Liu, F. Formation of a double diamond cubic phase by thermotropic liquid crystalline self-assembly of bundled bolaamphiphiles. *Angew. Chem.* **2016**, *128* (29), 8464−8467.
(14) Liu, F.; Prehm, M.; Zeng, X.; Tschierske, C.; Ungar, G. Skeletal cubic, lamellar, and ribbon phases of bundled thermotropic bolapolyphiles. *J. Am. Chem. Soc.* **2014**, *136* (19), 6846−6849.
(15) Goodby, J. W.; Görtz, V.; Cowling, S.; Mackenzie, G.; Martin, P.; Plusquellec, D.; Benvegnu, T.; Boullanger, P.; Lafont, D.; Queneau, Y. Thermotropic liquid crystalline glycolipids. *Chem. Soc. Rev.* **2007**, *36* (12), 1971−2032.
(16) Hashim, R.; Sugimura, A.; Minamikawa, H.; Heidelberg, T. Nature-like synthetic alkyl branched-chain glycolipids: a review on chemical structure and self-assembly properties. *Liq. Cryst.* **2012**, *39* (1), 1−17.
(17) Nowak, S. R.; Lachmayr, K. K.; Yager, K. G.; Sita, L. R. Stable thermotropic 3D and 2D double gyroid nanostructures with sub-2-nm feature size from scalable sugar−polyolefin conjugates. *Angew. Chem., Int. Ed.* **2021**, *133* (16), 8792−8798.
(18) van Doren, H.; Buma, T.; Kellogg, R. M.; Wynberg, H. Carbohydrate liquid crystals even at ambient temperature. *J. Chem. Soc., Chem. Commun.* **1988**, *7*, 460−462.
(19) Shearman, G. C.; Khoo, B. J.; Motherwell, M.-L.; Brakke, K. A.; Ces, O.; Conn, C. E.; Seddon, J. M.; Templer, R. H. Calculations of and evidence for chain packing stress in inverse lyotropic bicontinuous cubic phases. *Langmuir* **2007**, *23* (13), 7276−7285.
(20) Matsen, M. W.; Bates, F. S. Origins of complex self-assembly in block copolymers. *Macromolecules* **1996**, *29* (23), 7641−7644.
(21) Reddy, A.; Dimitriyev, M. S.; Grason, G. M. Medial packing and elastic asymmetry stabilize the double-gyroid in block copolymers. *Nat. Commun.* **2022**, *13* (1), 2629.
(22) Baccile, N.; Seyrig, C.; Poirier, A.; Alonso-de Castro, S.; Roelants, S. L.; Abel, S. Self-assembly, interfacial properties, interactions with macromolecules and molecular modelling and simulation of microbial bio-based amphiphiles (biosurfactants). *A tutorial review. Green Chem.* **2021**, *23* (11), 3842−3944.
(23) Borisch, K.; Diele, S.; Göring, P.; Kresse, H.; Tschierske, C. Tailoring thermotropic cubic mesophases: amphiphilic polyhydroxy derivatives. *J. Mater. Chem.* **1998**, *8* (3), 529−543.
(24) Zahid, N. I.; Conn, C. E.; Brooks, N. J.; Ahmad, N.; Seddon, J. M.; Hashim, R. Investigation of the effect of sugar stereochemistry on biologically relevant lyotropic phases from branched-chain synthetic glycolipids by small-angle X-ray scattering. *Langmuir* **2013**, *29* (51), 15794−15804.
(25) Von Minden, H.; Brandenburg, K.; Seydel, U.; Koch, M.; Garamus, V.; Willumeit, R.; Vill, V. Thermotropic and lyotropic properties of long chain alkyl glycopyranosides. Part II. Disaccharide headgroups. *Chem. Phys. Lipids* **2000**, *106* (2), 157−179.
(26) Shu, Q.; Lou, H.; Wei, T.; Liu, X.; Chen, Q. Contributions of glycolipid biosurfactants and glycolipid-modified materials to antimicrobial strategy: A review. *Pharmaceutics* **2021**, *13* (2), 227.
(27) Hashim, R.; Hashim, H. H. A.; Rodzi, N. Z. M.; Hussen, R. S. D.; Heidelberg, T. Branched chain glycosides: Enhanced diversity for phase behavior of easily accessible synthetic glycolipids. *Thin Solid Films* **2006**, *509* (1−2), 27−35.
(28) Kegel, L. L.; Szabó, L. Z.; Polt, R.; Pemberton, J. E. Alkyl melibioside and alkyl cellobioside surfactants: effect of sugar headgroup and alkyl chain length on performance. *Green Chem.* **2016**, *18* (16), 4446−4460.
(29) Lindsay, A. P.; Mueller, A. J.; Mahanthappa, M. K.; Lodge, T. P.; Bates, F. S. *1D SAXS Indexing Macro for Igor Pro*; Retrieved from the Data Repository for the University of Minnesota, 2021. https://doi.org/10.13020/9m8p-pv93 (last accessed 22 Dec 2023)
(30) Nguan, H.; Heidelberg, T.; Hashim, R.; Tiddy, G. Quantitative analysis of the packing of alkyl glycosides: a comparison of linear and branched alkyl chains. *Liq. Crys.* **2010**, *37* (9), 1205−1213.
(31) Chu, S. S.; Jeffrey, G. The refinement of the crystal structures of *β*-D-glucose and cellobiose. *Acta Crystallogr. B: Struct. Sci. Cryst.* **1968**, *24* (6), 830−838.
(32) Outcalt, S.; Laesecke, A.; Fortin, T. J. Density and speed of sound measurements of hexadecane. *J. Chem. Thermodyn.* **2010**, *42* (6), 700−706.
(33) Raman, E. P.; Guvench, O.; MacKerell, A. D., Jr CHARMM additive all-atom force field for glycosidic linkages in carbohydrates involving furanoses. *J. Phys. Chem. B* **2010**, *114* (40), 12981−12994.
(34) Guvench, O.; Mallajosyula, S. S.; Raman, E. P.; Hatcher, E.; Vanommeslaeghe, K.; Foster, T. J.; Jamison, F. W.; MacKerell, A. D., Jr CHARMM additive all-atom force field for carbohydrate derivatives and its utility in polysaccharide and carbohydrate−protein modeling. *J. Chem. Theory Comput.* **2011**, *7* (10), 3162−3180.
(35) Jo, S.; Kim, T.; Iyer, V. G.; Im, W. CHARMM-GUI: a web-based graphical user interface for CHARMM. *J. Comput. Chem.* **2008**, *29* (11), 1859−1865.
(36) Lee, J.; Patel, D. S.; Ståhle, J.; Park, S.-J.; Kern, N. R.; Kim, S.; Lee, J.; Cheng, X.; Valvano, M. A.; Holst, O. CHARMM-GUI membrane builder for complex biological membrane simulations with glycolipids and lipoglycans. *J. Chem. Theory Comput.* **2018**, *15* (1), 775−786.
(37) Martin, M. G.; Siepmann, J. I. Transferable potentials for phase equilibria. 1. United-atom description of n-alkanes. *J. Phys. Chem. B* **1998**, *102* (14), 2569−2577.
(38) Chen, B.; Potoff, J. J.; Siepmann, J. I. Monte Carlo calculations for alcohols and their mixtures with alkanes. Transferable potentials for phase equilibria. 5. United-atom description of primary, secondary, and tertiary alcohols. *J. Phys. Chem. B* **2001**, *105* (15), 3093−3104.
(39) Stubbs, J. M.; Potoff, J. J.; Siepmann, J. I. Transferable potentials for phase equilibria. 6. United-atom description for ethers, glycols, ketones, and aldehydes. *J. Phys. Chem. B* **2004**, *108* (45), 17596−17605.
(40) Martínez, L.; Andrade, R.; Birgin, E. G.; Martínez, J. M. PACKMOL: A package for building initial configurations for molecular dynamics simulations. *J. Comput. Chem.* **2009**, *30* (13), 2157−2164.
(41) Van Der Spoel, D.; Lindahl, E.; Hess, B.; Groenhof, G.; Mark, A. E.; Berendsen, H. J. GROMACS: fast, flexible, and free. *J. Comput. Chem.* **2005**, *26* (16), 1701−1718.
(42) Berendsen, H. J.; Postma, J. V.; Van Gunsteren, W. F.; DiNola, A.; Haak, J. R. Molecular dynamics with coupling to an external bath. *J. Chem. Phys.* **1984**, *81* (8), 3684−3690.
(43) Benito-Alifonso, D.; Galan, M. C. Brønsted-and Lewis-Acid-Catalyzed Glycosylation. In *Selective Glycosylations: Synthetic Methods and Catalysts*; Bennet, C., Ed.; Wiley-VCH, 2017; pp 155−172.
(44) Mazur, A. W.; Hiler, G. D., Jr Efficient preparation of benzyl glycosides of lactose and cellobiose using stannic chloride. *Carbohydr. Res.* **1987**, *168* (1), 146−150.
(45) Vill, V.; Vill, V.; Böcker, T.; Thiem, J.; Fischer, F. The stereochemistry of glycolipids. A key for understanding membrane functions *Liq. cryst.* **2006**, *33* (11−12), 1351−1358.
(46) Saari, N. N.; Mislan, A. A.; Hashim, R.; Zahid, N. I. Self-assembly, thermotropic, and lyotropic phase behavior of guerbet branched-chain maltosides. *Langmuir* **2018**, *34* (30), 8962−8974.
(47) Ogawa, S.; Asakura, K.; Osanai, S. Thermotropic and glass transition behaviors of n-alkyl *β*-D-glucosides. *RSC Adv.* **2013**, *3* (44), 21439−21446.

https://doi.org/10.1021/acs.biomac.3c01266
Biomacromolecules 2024, 25, 1291−1302

(48) Ericsson, C. A.; Ericsson, L. C.; Ulvenlund, S. Solid-state phase behaviour of dodecylglycosides. *Carbohydr. Res.* **2005**, *340* (8), 1529−1537.
(49) Hatakeyama, T.; Yoshida, H.; Nagasaki, C.; Hatakeyama, H. Differential scanning calorimetric studies on phase transition of glucose and cellulose oligosaccharides. *Polymer* **1976**, *17* (7), 559−562.
(50) Hashim, R.; Mirzadeh, S. M.; Heidelberg, T.; Minamikawa, H.; Yoshiaki, T.; Sugimura, A. A reevaluation of the epimeric and anomeric relationship of glucosides and galactosides in thermotropic liquid crystal self-assemblies. *Carbohydr. Res.* **2011**, *346* (18), 2948−2956.
(51) Ahmadi, S.; ManickamAchari, V.; Hussain, Z.; Hashim, R. Epimeric and anomeric relationship of octyl-α-D-gluco/galactosides: Insight from density functional theory and atom in molecules studies. *Comput. Theor. Chem.* **2017**, *1108*, 93−102.
(52) Hashim, R.; Zahid, N. I.; Aripin, N. F. K.; Ogawa, S.; Sugimura, A. Dry thermotropic glycolipid self-assembly: A review. *J. Oleo Sci.* **2018**, *67* (6), 651−668.
(53) Loo, Y.-L.; Register, R. A.; Adamson, D. H.; Ryan, A. J. A highly regular hexagonally perforated lamellar structure in a quiescent diblock copolymer. *Macromolecules* **2005**, *38* (11), 4947−4949.
(54) Zhou, N.; Lodge, T. P.; Bates, F. S. Phase behavior of polyisoprene-poly (butylene oxide) and poly (ethylene-*alt*-propylene)-poly (butylene oxide) block copolymers. *Soft Matter* **2010**, *6* (6), 1281−1290.
(55) Hillmyer, M. A.; Bates, F. S.; Almdal, K.; Mortensen, K.; Ryan, A. J.; Fairclough, J. P. A. Complex phase behavior in solvent-free nonionic surfactants. *Science* **1996**, *271* (5251), 976−978.
(56) Scalfani, V. F.; Bailey, T. S. Thermally stable photocuring chemistry for selective morphological trapping in block copolymer melt systems. *Chem. Mater.* **2010**, *22* (21), 5992−6000.
(57) Leibler, L. Theory of microphase separation in block copolymers. *Macromolecules* **1980**, *13* (6), 1602−1617.
(58) Matsen, M. W. Effect of architecture on the phase behavior of AB-type block copolymer melts. *Macromolecules* **2012**, *45* (4), 2161−2165.
(59) Khandpur, A. K.; Foerster, S.; Bates, F. S.; Hamley, I. W.; Ryan, A. J.; Bras, W.; Almdal, K.; Mortensen, K. Polyisoprene-polystyrene diblock copolymer phase diagram near the order-disorder transition. *Macromolecules* **1995**, *28* (26), 8796−8806.
(60) Abetz, V.; Simon, P. F. *Phase behaviour and morphologies of block copolymers*; Springer, 2005.
(61) Tschierske, C. Non-conventional liquid crystals—the importance of micro-segregation for self-organisation. *J. Mater. Chem.* **1998**, *8* (7), 1485−1508.
(62) Tschierske, C. Micro-segregation, molecular shape and molecular topology−partners for the design of liquid crystalline materials with complex mesophase morphologies. *J. Mater. Chem.* **2001**, *11* (11), 2647−2671.
(63) Liberman, L.; Coughlin, M. L.; Weigand, S.; Edmund, J.; Bates, F. S.; Lodge, T. P. Impact of side-chain length on the self-assembly of linear-bottlebrush diblock copolymers. *Macromolecules* **2022**, *55* (12), 4947−4955.
(64) Sakya, P.; Seddon, J. Thermotropic and lyotropic phase behaviour of monoalkyl glycosides. *Liq. Cryst.* **1997**, *23* (3), 409−424.
(65) Dorset, D. L.; Rosenbusch, J. P. Solid state properties of anomeric 1-*O*-n-octyl-D-glucopyranosides. *Chem. Phys. Lipids* **1981**, *29* (4), 299−307.
(66) Jeffrey, G. A.; Bhattacharjee, S. Carbohydrate liquid-crystals. *Carbohydr. Res.* **1983**, *115*, 53−58.
(67) Goodby, J. Liquid crystal phases exhibited by some monosaccharides. *Mol. Cryst. Liq.* **1984**, *110* (1−4), 205−219.
(68) Hoffmann, B.; Milius, W.; Voss, G.; Wunschel, M.; van Smaalen, S.; Diele, S.; Platz, G. Crystal structures and thermotropic properties of alkyl α-*D*-glucopyranosides and their hydrates. *Carbohydr. Res.* **1999**, *323* (1−4), 192−201.
(69) Mannock, D. A.; Collins, M. D.; Kreichbaum, M.; Harper, P. E.; Gruner, S. M.; McElhaney, R. N. The thermotropic phase behaviour and phase structure of a homologous series of racemic β-*D*-galactosyl dialkylglycerols studied by differential scanning calorimetry and X-ray diffraction. *Chem. Phys. Lipids* **2007**, *148* (1), 26−50.
(70) Manickam Achari, V.; Nguan, H. S.; Heidelberg, T.; Bryce, R. A.; Hashim, R. Molecular dynamics study of anhydrous lamellar structures of synthetic glycolipids: Effects of chain branching and disaccharide headgroup. *J. Phys. Chem. B* **2012**, *116* (38), 11626−11634.
(71) Goodby, J. W.; Watson, M. J.; Mackenzie, G.; Kelly, S. M.; Bachir, S.; Bault, P.; Gode, P.; Goethals, G.; Martin, P.; Ronco, G. The dependence of mesomorphic behaviour on the extent of hydrogen-bonding in sugar derived polyols. *Liq. Cryst.* **1998**, *25* (2), 139−147.
(72) Chong, T. T.; Heidelberg, T.; Hashim, R.; Gary, S. Computer modelling and simulation of thermotropic and lyotropic alkyl glycoside bilayers. *Liq. Cryst.* **2007**, *34* (2), 267−281.
(73) Ahmadi, S.; Manickam Achari, V.; Nguan, H.; Hashim, R. Atomistic simulation studies of the α/β-glucoside and galactoside in anhydrous bilayers: effect of the anomeric and epimeric configurations. *J. Mol. Model.* **2014**, *20*, 2165.
(74) Mondal, J.; Mahanthappa, M.; Yethiraj, A. Self-assembly of gemini surfactants: a computer simulation study. *J. Phys. Chem. B* **2013**, *117* (16), 4254−4262.
(75) Kulkarni, C. V.; Tang, T.-Y.; Seddon, A. M.; Seddon, J. M.; Ces, O.; Templer, R. H. Engineering bicontinuous cubic structures at the nanoscale—the role of chain splay. *Soft Matter* **2010**, *6* (14), 3191−3194.
(76) Imai, M.; Kawaguchi, A.; Saeki, A.; Nakaya, K.; Kato, T.; Ito, K.; Amemiya, Y. Fluctuations of lamellar structure prior to a lamellar gyroid transition in a nonionic surfactant system. *Phys. Rev. E* **2000**, *62* (5), 6865.
(77) Imai, M.; Nakaya, K.; Kawakatsu, T.; Seto, H. Dynamical nature of least stable fluctuation modes of lamellar structure observed in a nonionic surfactant/water system. *J. Chem. Phys.* **2003**, *119* (15), 8103−8111.
(78) Qi, S.; Wang, Z.-G. Kinetics of phase transitions in weakly segregated block copolymers: Pseudostable and transient states. *Phys. Rev. E* **1997**, *55* (2), 1682.
(79) Laradji, M.; Shi, A.-C.; Desai, R. C.; Noolandi, J. Stability of ordered phases in weakly segregated diblock copolymer systems. *Phys. Rev. Lett.* **1997**, *78* (13), 2577.
(80) Kuzmin, P. I.; Zimmerberg, J.; Chizmadzhev, Y. A.; Cohen, F. S. A quantitative model for membrane fusion based on low-energy intermediates. *Proc. Natl. Acad. Sci. U. S. A.* **2001**, *98* (13), 7235−7240.
(81) Wang, X.; Deserno, M. Determining the lipid tilt modulus by simulating membrane buckles. *J. Phys. Chem. B* **2016**, *120* (26), 6061−6073.

https://doi.org/10.1021/acs.biomac.3c01266
Biomacromolecules 2024, 25, 1291−1302